Paramagnetic Nd sublattice and thickness-dependent ferromagnetism in Nd₂NiMnO₆ double perovskite thin films

Jonathan Spring ⓘ,[1] Gabriele De Luca ⓘ,[2] Simon Jöhr,[1] Javier Herrero-Martín ⓘ,[3] Charles Guillemard ⓘ,[3,*]
Cinthia Piamonteze ⓘ,[4] Carlos M. M. Rosário ⓘ,[5,†] Hans Hilgenkamp ⓘ,[5] and Marta Gibert ⓘ[6]

[1]*Physik-Institut, University of Zurich, 8057 Zurich, Switzerland*
[2]*Institut de Ciència de Materials de Barcelona (ICMAB-CSIC), 08193 Bellaterra (Barcelona), Spain*
[3]*ALBA Synchrotron Light Source, Cerdanyola del Vallès 08290, Spain*
[4]*Swiss Light Source, Paul Scherrer Institut, 5232 Villigen, Switzerland*
[5]*Faculty of Science and Technology and MESA+ Institute for Nanotechnology, University of Twente, 7500 AE Enschede, The Netherlands*
[6]*Institute of Solid State Physics, TU Wien, 1040 Vienna, Austria*

We investigate ferromagnetic and insulating thin films of the *B*-site ordered double perovskite Nd_2NiMnO_6 (NNMO) grown by radio frequency off-axis magnetron sputtering. The films grow epitaxially strained on a selection of substrates and display a strain-independent and bulklike T_C of 200 K at a thickness of 30 unit cells. We explore the thickness dependence of the $NNMO/SrTiO_3(001)$ system and find ferromagnetism down to ultralow thicknesses of only 3 unit cells (~ 1.2 nm). Below 10 unit cells, the magnetic properties deteriorate due to an interfacial charge transfer caused by the polar discontinuity at the $NNMO/SrTiO_3$ interface. A detailed x-ray magnetic circular dichroism study allows us to separate the magnetic components into a robust ferromagnetic Ni/Mn sublattice and a paramagnetic Nd sublattice.

I. INTRODUCTION

B-site ordered double perovskites of the form RE_2NiMnO_6 (RE = rare earth) are an intriguing type of perovskite oxides as they feature the rare combination of electrically insulating behavior and ferromagnetism [1]. Next to RE_2NiMnO_6 this combination can, for example, be found in ultrathin $La_{0.9}Ba_{0.1}MnO_3$ films or in other ordered double perovskites such as $Sr_2Fe_{1+x}Re_{1-x}O_6$ [2,3]. Ferromagnetic insulators are promising for spintronics applications where they can generate spin currents [4]. Further, the emergence of hybrid improper ferroelectricity was predicted for artificial superlattices of two RE_2NiMnO_6 compounds with different REs. Combined with the well-established ferromagnetism, this would result in highly sought-after multiferroicity [5].

In RE_2NiMnO_6, charge transfer between the ordered Mn and Ni ions leads to a valence of Ni^{2+} and Mn^{4+} [6]. Hence, Ni is in a $3d^8$ and Mn in a $3d^3$ valence state. According to the Goodenough-Kanamori rules, oxygen-mediated superexchange is predicted to be ferromagnetic for this d^8-d^3

configuration with a $180°$ bond angle [7]. Considering all possible RE elements, the highest Curie temperature (T_C) of 280 K is realized in La_2NiMnO_6, which has the smallest octahedron distortions and hence the largest Ni-O-Mn bond angle of the series [8]. As we go toward smaller rare earth ions on the *A* site, the structural distortions increase, and the Ni-O-Mn bond angle decreases, manifesting in a steady reduction in T_C [1].

Here, we will focus on the member Nd_2NiMnO_6 (NNMO) with a bulk T_C of 194 K [1]. As do all the other RE_2NiMnO_6 oxides, NNMO crystallizes in the monoclinic space group $P2_1/n$, as illustrated in Fig. 1. This is derived from an orthorhombic *Pbnm* unit cell through a symmetry reduction associated with the *B*-site ordering [9]. Compared to the much more investigated La_2NiMnO_6, NNMO shows a more complex magnetic behavior as it contains magnetically active Nd^{3+} on the *A*-site in addition to the ferromagnetic Ni/Mn *B*-site sublattice. While the exact nature of this additional interaction remains under discussion, it is generally agreed upon that it leads to a decrease in the total magnetization at very low temperatures [1,10–14]. Asai *et al.* ascribed this to a negative superexchange interaction between Ni and Nd [10]. Later, Booth *et al.* suggested a magnetocrystalline anisotropy [1]. Sánchez-Benítez *et al.* proposed an antiferromagnetic ordering of Nd with respect to the exchange field of the transition metals [12]. Finally, Pal *et al.* proposed a different mechanism in which Nd displays paramagnetic behavior [14]. In the ground state, the paramagnetic Nd spin moments will align parallel to the ferromagnetic spin-dominated Ni/Mn sublattice. As Nd^{3+} has a less than half-filled valence shell, according to Hund's third rule, the total angular momentum
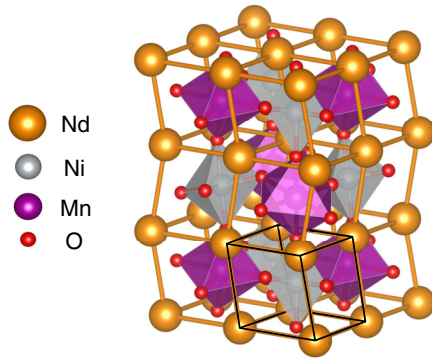

FIG. 1. Crystal structure of NNMO in the monoclinic $P2_1/n$ phase. The pseudocubic unit cell is overlaid in black. Structural data from [13].

has to be minimized ($J = L - S$). Hence, the orbital and spin magnetic moments are aligned antiparallel. Further, as for most $4f$ ions, its total moment is dominated by the orbital component [15]. Accordingly, the Nd total magnetic moment will be antiparallel to that of Ni/Mn, diminishing the total magnetic moment of NNMO.

So far, NNMO research has focused almost exclusively on bulk samples, and only a very limited number of reports on thin films are available [16,17]. Further, these films are relatively thick (> 150 nm) and high-quality two-dimensional growth has not been reported so far. Here we employ radio frequency (rf) off-axis magnetron sputtering in combination with *in situ* reflection high-energy electron diffraction (RHEED) to grow NNMO films on various perovskite oxide substrates. Using x-ray magnetic circular dichroism (XMCD), we demonstrate the coexistence of a ferromagnetic Ni/Mn and a paramagnetic Nd sublattice. While interfacial charge transfer effects impair the magnetic properties in the ultrathin limit, we find ferromagnetism down to thicknesses of at least three pseudocubic (pc) unit cells (uc).

II. MATERIALS AND METHODS

A. Growth and structural characterization

The growth of the NNMO thin films was carried out by radio-frequency off-axis magnetron sputtering in a custom-built growth chamber equipped with *in situ* RHEED. We adopt the inverted magnetron geometry to combine RHEED with magnetron sputtering as first described by Podkaminer *et al.* [18]. We find that it is crucial to equip our system with a loadlock to avoid exposure of the NNMO target to the outside atmosphere. Without loadlock, reproducible growth of NNMO was not possible. The single-crystal substrates are heated to a temperature of $660 - 680\,^\circ$C in the growth atmosphere of 0.1 mbar with a constant gas flow of 35 SCCM Ar and 10 SCCM O_2 (SCCM denotes cubic centimeter per minute at STP). The deposition is carried out from a 2-in. stoichiometric NNMO target at a plasma rf power of 35 W. Finally, the sample is cooled to room temperature in the growth atmosphere.

X-ray diffraction is performed on a Rigaku SmartLab diffractometer equipped with a Ge (220) monochromator us-

ing Cu $K\alpha_1$ radiation (1.5406 Å). Lattice parameter and film thickness were fitted to the measured data using the Inter-activeXRDFit MATLAB tool [19]. Topography images were obtained on a Park Systems NX10 atomic force microscope and evaluated using GWYDDION 2.58.

B. Magnetic characterization

Magnetic properties were investigated using both a Quantum Design MPMS3 SQUID (superconducting quantum interference device) magnetometer and a Quantum Design physical property measurement system fitted with the vibrating-sample magnetometer option.

Scanning SQUID microscopy was performed with the sample and the scan head submerged in liquid He. The SQUID pickup loop with an effective area of 27 μm^2 is brought into contact with the sample surface at an angle of $15\,^\circ$. It is scanned over the surface and picks up the change in local magnetic flux. Even though the scanning SQUID mainly picks up on the out-of-plane flux, the imaged regions do not necessarily possess out-of-plane magnetization, as also in-plane magnetization produces stray fields with an out-of-plane component.

C. XAS and XMCD

X-ray absorption spectroscopy (XAS) and XMCD measurements were carried out at the BOREAS beamline at the ALBA synchrotron in Barcelona, Spain [20] and the X-Treme beamline at the Swiss Light Source SLS in Villigen, Switzerland [21]. Data was acquired in grazing incidence ($60\,^\circ$ to the sample normal) using total electron yield detection. No samples on $DyScO_3$ (DSO) substrates were measured, as the strong paramagnetism of these substrates leads to the risk of losing the sample in the cryostat at high applied fields.

The 300 K XAS data is obtained by taking the sum of absorption data from linearly vertically and horizontally polarized light, which is subsequently normalized to the most intense peak. The Mn reference spectra were obtained on the following powder samples: $MnCl_2$ (Mn^{2+}), Mn_2O_3 (Mn^{3+}), and $SrMnO_3$ (Mn^{4+}). For Ni we used NiO (Ni^{2+}) and $NdNiO_3$ (Ni^{3+}).

The low-temperature XMCD spectra are obtained by calculating the difference between absorption spectra recorded with circularly right- and left-hand polarized light. The obtained spectra were then normalized by the maximum intensity of the respective XAS measurement. XMCD asymmetry loops were attained by alternatingly measuring the x-ray absorption at an on- and off-resonance energy of the respective edge while sweeping the magnetic field. This procedure was carried out twice with circularly left- and right-hand polarized x-rays. To obtain quantitative magnetic moments from the XMCD measurements, we applied the orbital and spin sum rules introduced by Carra *et al.* [22]. Additional details on applying the sum rules can be found in the Supplemental Material [23].

III. RESULTS AND DISCUSSION

A. Structural and electronic properties

NNMO thin films were grown by off-axis rf magnetron sputtering on six different substrates in $(001)_{pc}$
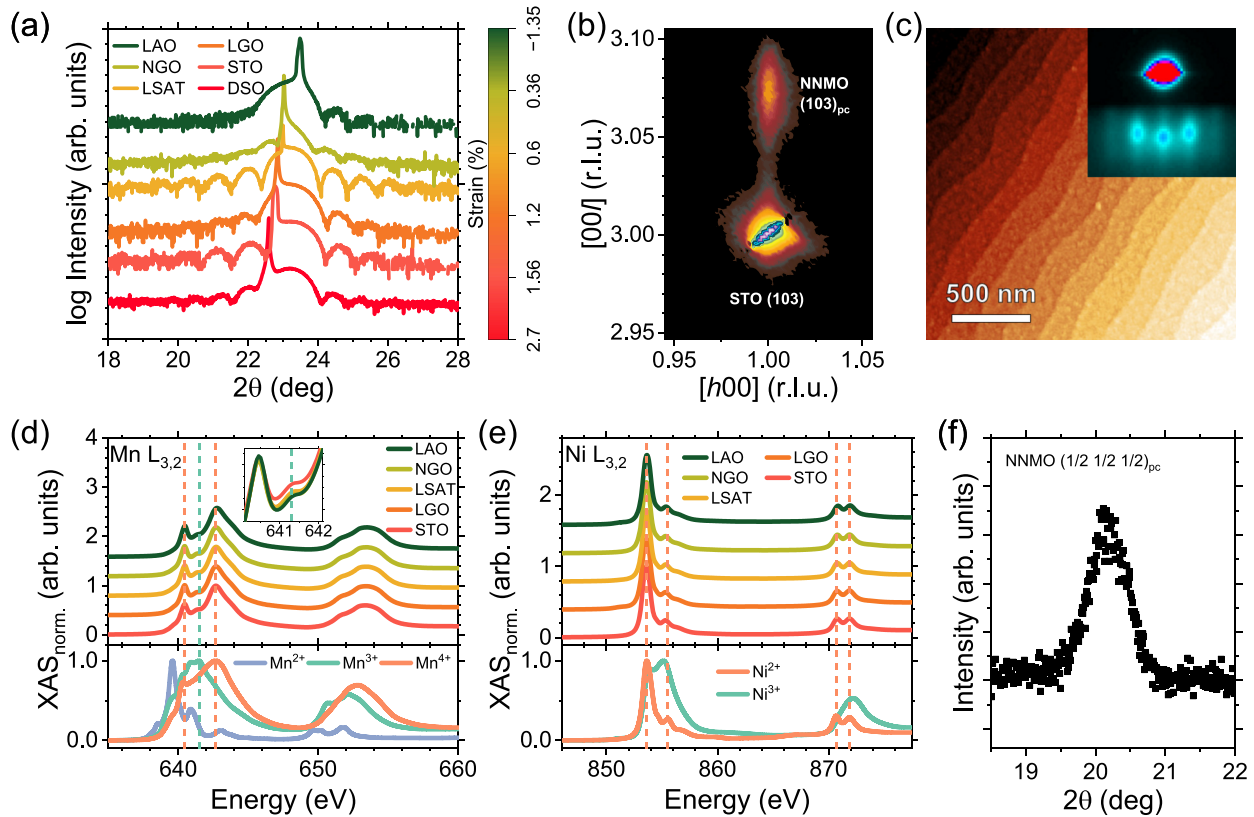
FIG. 2. Structural and electronic characterization of NNMO thin films on different substrates. (a) X-ray diffraction around the $(001)_{pc}$ substrate peaks. Finite-size Laue oscillations indicate high crystal quality and epitaxial growth on all substrates. The color scale indicates the extent of epitaxial strain. (b) Reciprocal space map around the (103) STO substrate peak indicating a fully strained NNMO film. (c) AFM topography of a NNMO/STO sample showing step-and-terrace morphology. Inset: The RHEED pattern of the as-grown film indicates a two-dimensional surface. (d) The top panel shows normalized XAS data around the Mn $L_{3,2}$ absorption edge. The inset presents a magnification around 641.3 eV. Note that the curves for the samples grown on NGO and LGO are hidden behind the curves for LAO and LSAT, respectively. The bottom panel shows reference XAS spectra for different Mn valence states. Vertical lines indicate the reference peak positions. All spectra were recorded at 300 K. (e) Same as (d) but around the Ni $L_{3,2}$ absorption edge. (f) The $(\frac{1}{2} \frac{1}{2} \frac{1}{2})_{pc}$ XRD peak is associated with the long-range ordering of the Ni/Mn sublattice.

orientation imposing varying degrees of epitaxial strain: $LaAlO_3$ (LAO; -1.33%), $NdGaO_3$ (NGO; $+0.38\%$), $(LaAlO_3)_{0.3}(Sr_2TaAlO_6)_{0.7}$ (LSAT; $+0.57\%$), $LaGaO_3$ (LGO; $+1.23\%$), $SrTiO_3$ (STO; $+1.59\%$), and $DyScO_3$ (DSO; $+2.73\%$). All substrates were annealed to induce step-and-terrace surface morphology. Additionally, the STO substrates are TiO_2 terminated. The strains are calculated using a pseudocubic lattice parameter of 3.844 Å for bulk NNMO derived from the monoclinic lattice parameters given in [8] (see the overlay in Fig. 1). The films have a thickness of 30 pseudocubic unit cells (~ 11.4 nm) if not explicitly stated otherwise. X-ray diffraction (XRD) around the $(001)_{pc}$ substrate peaks features finite-size Laue oscillations indicating high-quality epitaxial growth on all substrates [Fig. 2(a)]. The film thickness is confirmed by fitting the Laue oscillations [19]. An exemplary reciprocal space map for a sample grown on STO shows that the film is coherently strained to the substrate with no discernible relaxation occurring over the thickness of 30 unit cells [Fig. 2(b)]. Reciprocal space maps for films on other substrates are shown in Supplemental Material Fig. S1

[23], also demonstrating coherent strain. Further, using atomic force microscopy (AFM), we show in Fig. 2(c) that the NNMO film inherits the well-defined step-and-terrace structure of the STO substrate. AFM topography images for the films grown on the other substrates are shown in Supplemental Material Fig. S2 [23]. This, together with the RHEED patterns collected after the film growth, e.g., for NNMO/STO in the inset of Fig. 2(c), attests to a two-dimensional growth mode of our thin films. The full RHEED intensity vs time graph is shown in Supplemental Material Fig. S3 [23]. The period of the RHEED oscillations is in agreement with the film thickness fitted from XRD.

To probe the electronic structure of the NNMO films, we resort to XAS. This allows us to determine the oxidation states on an element basis. In Figs. 2(d) and 2(e) we present XAS data recorded around the Mn and Ni $L_{3,2}$ absorption edges in the top panels together with reference data for selected Mn and Ni oxidation states in the bottom panels. Note that no NNMO/DSO sample was measured. Looking at the Mn XAS, we conclude that all films feature predominantly Mn^{4+} independent of strain. However, we can also appreciate a
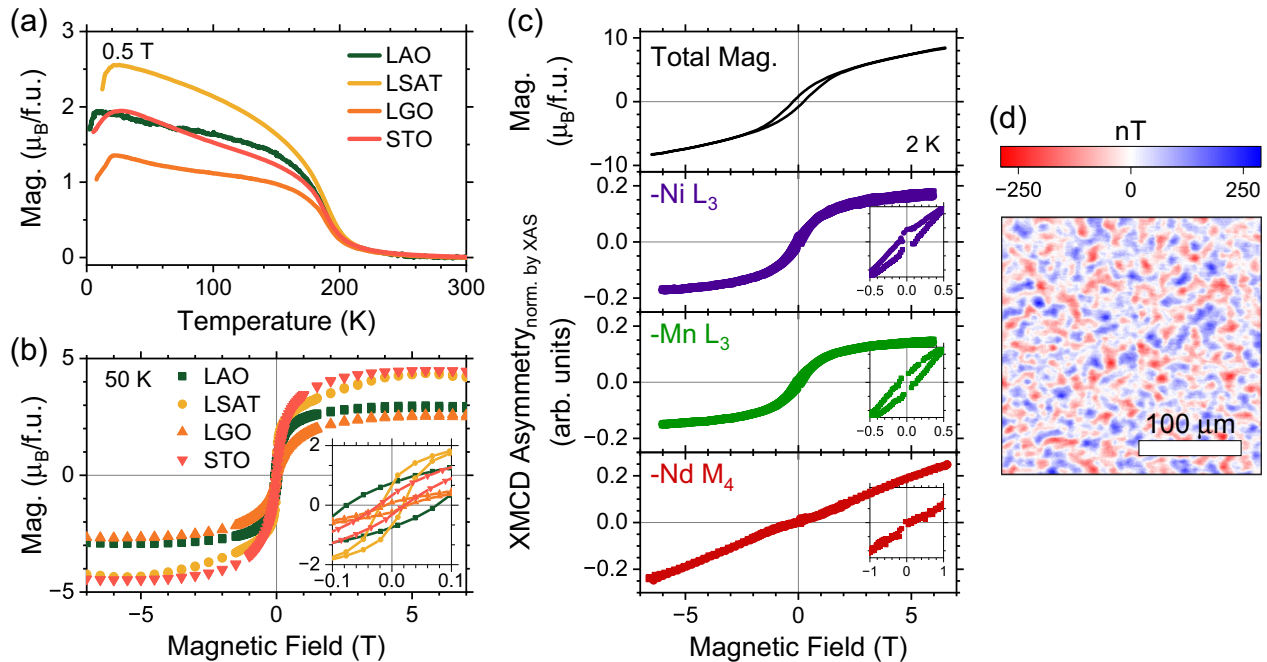
FIG. 3. Magnetic characterization of 30 uc NNMO thin films on different substrates. (a) Magnetization as a function of temperature in field cooling at an applied field of 0.5 T. All samples show a bulklike T_C of ∼200 K and feature a downturn in magnetization at low temperatures. (b) Magnetization as a function of the applied magnetic field at a temperature of 50 K. (c) Magnetization versus applied field for an NNMO/STO sample measured at ∼2 K. Top panel: Total magnetization. Lower panels: Elemental contributions to the total magnetization for Ni, Mn, and Nd are illustrated by the respective XMCD asymmetry. The insets show a magnification around 0 T. We plot minus the XMCD values for easier comparison to the total magnetization data. (d) Magnetic field distribution on the surface of an NNMO film grown on STO imaged by scanning SQUID microscopy at 4.2 K and 0 T.

small contribution of Mn^{3+} to the measured XAS spectra at 641.3 eV. Closer inspection of the L_3 edge reveals that the Mn^{3+} content is marginally larger on the STO sample [Fig. 2(d), inset]. This can most likely be attributed to an interfacial charge transfer caused by the polar discontinuity between STO and NNMO, as we will discuss later. Recently, we have reported on this phenomenon in La_2NiMnO_6 thin films [24,25]. The Ni XAS, on the other hand, indicates an almost pure valence state of Ni^{2+} with no appreciable difference between films grown on different substrates. Hence, all our NNMO films feature an almost pure Mn^{4+}/Ni^{2+} valence configuration. This is in accordance with what one expects for a well-ordered double perovskite structure [6].

B-site ordering leads to the formation of alternating Ni^{2+} and Mn^{4+} planes in the $(111)_{pc}$ direction (see Fig. 1), effectively doubling the periodicity. In La_2NiMnO_6/STO, where the ordering was directly confirmed by transmission electron microscopy, the emergence of a $(\frac{1}{2}\frac{1}{2}\frac{1}{2})_{pc}$ XRD peak was associated with this doubling along $(111)_{pc}$ [24]. Here, we perform XRD along $(111)_{pc}$ on a 60-uc NNMO film grown on STO. The resulting $(\frac{1}{2}\frac{1}{2}\frac{1}{2})_{pc}$ XRD peak is presented in Fig. 2(f), further indicating *B*-site ordering. The full 2θ scan is presented in Supplemental Material Fig. S4 [23]. However, we cannot exclude the possibility of *A*-site displacements contributing to the XRD signal [26].

Finally, we confirm the insulating nature of NNMO thin films through a room temperature four-point van der Pauw measurement on a 30 uc film grown on STO(001), which

results in a resistivity of 1.4 kΩcm. This is very close to what was found for La_2NiMnO_6 thin films, which are also ferromagnetic insulators [24].

B. Magnetic properties

As the just-validated rocksalt ordering of the Ni^{2+}/Mn^{4+} sublattice is associated with ferromagnetism, we now turn to magnetization measurements. Figure 3(a) shows magnetization per formula unit (f.u.) of NNMO vs temperature measurements at an applied in-plane magnetic field of 0.5 T for NNMO films grown on different substrates. Substrate contributions were removed by premeasuring $M(T)$ for each substrate before the film growth. No data for samples on DSO and NGO substrates is presented as they contribute a large paramagnetic signal that cannot be properly removed even by premeasuring the substrate. First, we determine a bulklike T_C of ∼200 K for all samples. Further, we ascertain the low-temperature downturn in the magnetization below ∼30 K on all NNMO films grown on different substrates. For the film on LAO, the onset of the downturn seems to occur at a slightly lower temperature. We find that the downturn changes into an upturn at applied fields larger than ∼1 T, as exemplified for STO in Supplemental Material Fig. S5 [23]. This is in accordance with what has already been reported on both bulk and thin film samples, and it must be connected to a form of alignment of the Nd magnetic moments below temperatures of around 30 K [10,16]. We will further discuss the nature of this downturn in the upcoming section. To characterize the
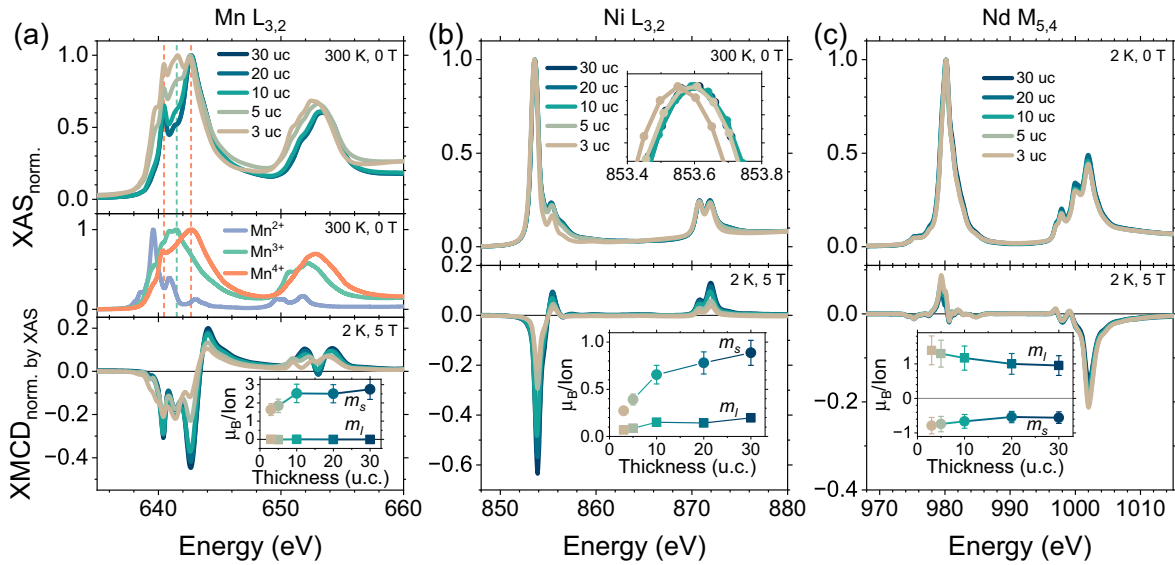
FIG. 4. Thickness-dependent XAS and XMCD data for NNMO/STO. (a) Top: XAS around the Mn $L_{3,2}$ edge. Comparison to the reference spectra in the middle panel shows a clear increase in Mn^{3+} content for films of 10 unit cells and less. Bottom: Mn XMCD spectra indicate a decrease in the magnetic moment for thinner films. The inset illustrates the orbital and spin magnetic moments extracted from the XMCD spectra using the sum rules. (b) Top: XAS around the Ni $L_{3,2}$ edge displays no appreciable change in Ni valence with film thickness. Bottom: XMCD shows a decreasing magnetic moment with decreasing film thickness. (c) Top: XAS at the Nd $M_{5,4}$ edge features no change in Nd valence as a function of sample thickness. Bottom: XMCD, in combination with the sum rules, indicates an increase in Nd spin and orbital moment with decreasing film thickness. Note that for Nd, in contrast to Ni and Mn, the two components are of opposite signs.

ferromagnetic nature of our NNMO thin films further, we present hysteresis loops in Fig. 3(b). The dia- and paramagnetic contributions are removed by subtracting a linear fit in the region above 4 T. On all substrates, the magnetic moment saturates at applied fields larger than ∼3 T, and we find a hysteretic opening around the origin.

To disentangle the different contributions to the total magnetization, we focus on an exemplary sample grown on STO in Fig. 3(c). The top panel shows the total magnetization hysteresis loop. In contrast to Fig. 3(b), this data was recorded at ∼2 K, well below the onset of the downturn shown in Fig. 3(a). For proper substrate removal, we measured the hysteresis loop of the bare substrate prior to the film growth and subtracted it from the film measurement. The result shows a hysteretic opening around zero field, as is typical for ferromagnets. However, unlike ferromagnets, we do not observe saturation of the magnetic moment at high applied fields. Instead, we find a linear paramagnetic behavior above ∼3 T. In the lower panels of Fig. 3(c), we present element-specific XMCD asymmetry loops recorded at the indicated absorption edges at 2 K. For Ni and Mn, we observe ferromagnetic behavior characterized by a hysteretic opening around 0 T (insets) and an almost saturating magnetic moment at high fields. On the other hand, the XMCD asymmetry for Nd features paramagnetic behavior with no signs of saturation. This is a direct visualization of purely paramagnetic rare earth ions in a ferromagnetic double perovskite matrix, and it corroborates the model of entirely paramagnetic Nd moments introduced by Pal *et al.* [14]. Note that Ni/Mn and Nd are measured at different absorption edges (L_3 for Ni/Mn and M_4 for Nd). The application of XMCD sum rules in the next section will shed more light on the orientation of the magnetic moments.

Finally, we use SQUID microscopy to visualize the spatial distribution of the magnetic fields emanating from the surface of an NNMO film grown on STO [Fig. 3(d)] [27]. These measurements are performed after cooling the sample to 4.2 K at zero applied magnetic field. We find regions of opposite signs and comparable magnitudes of ∼290 nT, which correspond to the local magnetic fields generated by the ferromagnetic domains of NNMO [28]. Over the whole scan, the measured field averages out to 0 T, as expected for a ferromagnet cooled below its T_C in zero field. Calculating the two-dimensional autocorrelation function indicates no preferential orientation of the domains.

C. Thickness dependence

After investigating NNMO films of bulklike thickness, we will now turn toward the ultrathin regime in a thickness-dependence study of films grown on STO ranging from 30 down to 3 uc. XRD measurements for the whole series are presented in Supplemental Material Fig. S6 [23]. In Fig. 4, we present the respective XAS and XMCD data. XAS on the Mn $L_{3,2}$ absorption edge indicates a strong thickness dependence of the Mn oxidation state [Fig. 4(a), top and middle panels]. For films of 10 uc and less, we detect an increasing concentration of Mn^{3+} compared to the almost pure Mn^{4+} state in bulklike films. As the employed total electron yield detection method is highly surface sensitive, the NNMO/STO interfacial region is not accessible in the thick films and has an increased relative weight in the measurements on thinner films. Hence, the detected Mn^{3+} must be preferentially located close to the interface between the film and the substrate. In the bottom panel of Fig. 4(a), we present the corresponding

XMCD data. We observe an unambiguous dichroic signal down to thicknesses of only 3 uc (~ 1.2 nm), attesting to the stability of the Ni/Mn ferromagnetic sublattice. However, with reduced thickness, we also find a reduced normalized XMCD signal and a decrease in T_C (Supplemental Material Fig. S7 [23]). The inset shows quantitative values for the Mn orbital and spin magnetic moments (m_l and m_s) obtained by applying the XMCD sum rules. We find that the spin component dominates the total moment and that the orbital moment is almost completely quenched, as expected for a $3d$ ion. For a bulklike 30-uc-thick film, we infer a Mn spin moment of $2.7\mu_B$/ion. This value is reduced with decreasing film thickness, with the largest reduction happening below 10 uc. The deterioration in the magnetic properties of ultrathin NNMO films is related to the increased weight of interfacial Mn^{3+}, which correlates with disorder in the Ni/Mn sublattice [25]. The increased disorder reduces the number of ferromagnetic superexchange interactions [8]. The increase in Mn^{3+} at the interface is most likely caused by an interfacial charge transfer triggered by the polar discontinuity between STO and NNMO, as is most famously known for the $LaAlO_3$/STO system [29]. Recently, we have reported in detail on this mechanism at the La_2NiMnO_6/STO interface [24,25]. Here, unlike for $LaAlO_3$/STO, the extra charge is transferred to the Mn site in the thin film instead of the Ti site in the substrate. This is similar to what was found at the $LaMnO_3$/STO interface [28]. Additional Mn $L_{3,2}$ XAS on 5-uc NNMO films grown on different substrates confirms this mechanism (Supplemental Material Fig. S8 [23]). On substrates that do not impose a polar discontinuity at the interface to the NNMO film (LAO, NGO, and LGO), Mn remains in a predominantly 4+ oxidation state even at the ultrathin limit. This also explains why we observed a minute Mn^{3+} signature for the 30-uc NNMO film on STO [inset of Fig. 2(d)] but not on the other substrates. LAO, NGO, and LGO do not feature a polar discontinuity at the interface to NNMO, and for LSAT, it is three times smaller than for STO. Finally, we point out that the NNMO films remain insulating down to the lowest thicknesses irrespective of the charge transfer, as exemplified by a room temperature resistivity of $7.6\,\mathrm{k\Omega cm}$ on a 5 uc film on STO.

Turning to XAS at the Ni $L_{3,2}$ edge [Fig. 4(b), top panel], the picture is somewhat different. We find no significant change in the Ni valence when reducing the film thickness, i.e., also close to the NNMO/STO interface, Ni stays in a predominantly 2+ oxidation state [cf. reference in Fig. 2(e)]. Only for the thinnest 3-uc sample do we observe a minute shift (~ 50 meV) of the L_3 edge toward lower energies indicating a slight reduction of the Ni valence state (inset). Still, the extra charge introduced to the system by the polar discontinuity is preferentially located on the Mn site. However, the magnetic moment of Ni^{2+} still shows a substantial reduction with decreasing film thickness [Fig. 4(b), bottom panel] due to the reduced number of ferromagnetic Ni^{2+}/Mn^{4+} superexchange interactions related to the interfacial Ni/Mn disorder [25]. As already shown for Mn, the Ni sum rule values for m_l and m_s (presented in the inset) show a dominant spin component. Reducing the thickness from 30 to 10 uc, we find a moderate reduction in both m_l and m_s, while the thickness effect

is much stronger below 10 uc. This is in accordance with the disorder-inducing interfacial charge transfer, which only becomes relevant in very thin films.

In Fig. 4(c), we present data on the Nd $M_{5,4}$ absorption edges. The XAS measurements in the top panel show a stable Nd^{3+} valence for all thicknesses. (Compare, for example, to bulk $NdNiO_3$ in [30].) The XMCD data in the lower panel shows a very different situation than for Ni and Mn. Applying the XMCD sum rules (inset) reveals that the orbital and spin components of the magnetic moment are aligned in opposite directions. This is expected for a rare earth with a less than half-filled $4f$ shell where, according to Hund's rules, the total angular momentum J has to be minimized. As the orbital magnetic moment m_l is larger in magnitude than the spin magnetic moment m_s, the direction of the total magnetic moment is determined by m_l. Comparing the sum rule data for all elements, we find that at 5 T, the total magnetic moments of Ni/Mn and Nd are aligned in parallel while their spin components are antiparallel. This means at low temperatures and high applied fields, the total moments of the Ni/Mn and Nd sublattices add up, as evidenced by the low-temperature upturn in $M(T)$ measurements at fields larger than 1 T (Supplemental Material Fig. S5 [23]). In the ground state (i.e., low applied field), the spin moments of the paramagnetic Nd ions will align in parallel to the spin moments of the ferromagnetic Ni/Mn sublattice via exchange coupling, as suggested by Pal *et al.* [14]. This leads to Nd total moments, dominated by their orbital component, that are antiparallel to the Ni/Mn moments and hence a decrease in the total magnetization, as seen in low-field $M(T)$ measurements [Fig. 3(a)]. This reversal of the Nd orbital and spin moments at low fields should be visible in XMCD measurements. However, after extensive XMCD studies, the reversal of the Nd moments could not be resolved experimentally. It is worth pointing out that this reversal was also not observed in bulk XMCD experiments [14]. Finally, looking at the thickness dependence of the Nd magnetic moments, the strong decrease with reduced film thickness observed for Ni and Mn is not found for the Nd moments [inset of Fig. 4(c)]. This robustness against the deterioration of magnetic properties in ultrathin films further confirms that the Nd ions are not part of the ferromagnetic sublattice. In fact, for both m_l and m_s, we find a slight increase in magnitude when reducing the film thickness. This points to a stabilizing effect of the sample's interfaces on the Nd alignment.

IV. CONCLUSIONS

We have demonstrated the sputter growth of high-quality NNMO thin films on a range of substrates. Magnetization measurements reveal a bulklike T_C of ~ 200 K in 30 unit cell films and a low-temperature downturn in magnetization. For samples on STO, we find clear evidence for ferromagnetism down to ultralow thicknesses of only 3 uc. However, the magnetic properties deteriorate strongly with reduced film thickness due to an interfacial charge transfer leading to an increased Mn^{3+} content inhibiting the ferromagnetic Ni^{2+}/Mn^{4+} superexchange. Through XMCD analysis, we could separate the ferromagnetic behavior of the Ni/Mn

sublattice from that of the paramagnetic Nd sublattice. By applying the XMCD sum rules, we find opposing Nd spin and orbital magnetic moments with the direction of the total Nd moment determined by the larger orbital component. At high applied fields, the Nd total moment is found to be parallel to that of the Ni/Mn sublattice.

[1] R. Booth, R. Fillman, H. Whitaker, A. Nag, R. Tiwari, K. Ramanujachary, J. Gopalakrishnan, and S. Lofland, An investigation of structural, magnetic and dielectric properties of R_2NiMnO_6 (R=rare earth, Y), Mater. Res. Bull. **44**, 1559 (2009).

[2] W. Li, B. Zhu, Q. He, A. Y. Borisevich, C. Yun, R. Wu, P. Lu, Z. Qi, Q. Wang, A. Chen, H. Wang, S. A. Cavill, K. H. L. Zhang, and J. L. MacManus-Driscoll, Interface engineered room-temperature ferromagnetic insulating state in ultrathin manganite films, Adv. Sci. **7**, 1901606 (2020).

[3] C. Sohn, E. Skoropata, Y. Choi, X. Gao, A. Rastogi, A. Huon, M. A. McGuire, L. Nuckols, Y. Zhang, J. W. Freeland, D. Haskel, and H. N. Lee, Room-temperature ferromagnetic insulating state in cation-ordered double-perovskite $Sr_2Fe_{1+x}Re_{1-x}O_6$ films, Adv. Mater. **31**, 1805389 (2019).

[4] M. Coll, J. Fontcuberta, M. Althammer, M. Bibes, H. Boschker, A. Calleja, G. Cheng, M. Cuoco, R. Dittmann, B. Dkhil, I. El Baggari, M. Fanciulli, I. Fina, E. Fortunato, C. Frontera, S. Fujita, V. Garcia, S. T. Goennenwein, C. G. Granqvist, J. Grollier *et al.*, Towards oxide electronics: A roadmap, Appl. Surf. Sci. **482**, 1 (2019).

[5] H. J. Zhao, W. Ren, Y. Yang, J. Íñiguez, X. M. Chen, and L. Bellaiche, Near room-temperature multiferroic materials with tunable ferromagnetic and electrical properties, Nat. Commun. **5**, 4021 (2014).

[6] G. Blasse, Ferromagnetic interactions in non-metallic perovskites, J. Phys. Chem. Solids **26**, 1969 (1965).

[7] J. Kanamori, Superexchange interaction and symmetry properties of electron orbitals, J. Phys. Chem. Solids **10**, 87 (1959).

[8] R. I. Dass, J. Q. Yan, and J. B. Goodenough, Oxygen stoichiometry, ferromagnetism, and transport properties of $La_{2-x}NiMnO_{6+\delta}$, Phys. Rev. B **68**, 064415 (2003).

[9] J. Blasco, M. Sánchez, J. Pérez-Cacho, J. Garcìa, G. Subìas, and J. Campo, Synthesis and structural study of $LaNi_{1-x}Mn_xO_{3+\delta}$ perovskites, J. Phys. Chem. Solids **63**, 781 (2002).

[10] K. Asai, K. Fujiyoshi, N. Nishimori, Y. Satoh, Y. Kobayashi, and M. Mizoguchi, Magnetic properties of $REMe_{0.5}Mn_{0.5}O_3$ (RE = Rare Earth Element, Me = Ni, Co), J. Phys. Soc. Jpn. **67**, 4218 (1998).

[11] C. Shi, Y. Hao, and Z. Hu, Local valence and physical properties of double perovskite Nd_2NiMnO_6, J. Phys. D: Appl. Phys. **44**, 245405 (2011).

[12] J. Sánchez-Benítez, M. J. Martínez-Lope, J. A. Alonso, and J. L. García-Muñoz, Magnetic and structural features of the $NdNi_{1-x}Mn_xO_3$ perovskite series investigated by neutron diffraction, J. Phys.: Condens. Matter **23**, 226001 (2011).

[13] W. Z. Yang, X. Q. Liu, H. J. Zhao, Y. Q. Lin, and X. M. Chen, Structure, magnetic, and dielectric characteristics of Ln_2NiMnO_6 (Ln = Nd and Sm) ceramics, J. Appl. Phys. **112**, 064104 (2012).

[14] S. Pal, S. Jana, S. Govinda, B. Pal, S. Mukherjee, S. Keshavarz, D. Thonig, Y. Kvashnin, M. Pereiro, R. Mathieu, P. Nordblad, J. W. Freeland, O. Eriksson, O. Karis, and D. D. Sarma, Peculiar magnetic states in the double perovskite Nd_2NiMnO_6, Phys. Rev. B **100**, 045122 (2019).

[15] J. Zhou and G. A. Fiete, Rare earths in a nutshell, Phys. Today **73** (1), 66 (2020).

[16] A. K. Singh, S. Chauhan, P. Balasubramanian, S. K. Srivastava, and R. Chandra, Influence of substrate induced strain on B-site ordering and magnetic properties of Nd_2NiMnO_6 epitaxial thin films, Thin Solid Films **629**, 49 (2017).

[17] G. Singh, P. Singh, R. J. Choudhary, and A. Dogra, Effect of oxygen pressure on structural and magnetic properties of Nd_2NiMnO_6 thin films grown on different substrates, J. Alloys Compd. **739**, 586 (2018).

[18] J. P. Podkaminer, J. J. Patzner, B. A. Davidson, and C. B. Eom, Real-time and *in situ* monitoring of sputter deposition with RHEED for atomic layer controlled growth, APL Mater. **4**, 086111 (2016).

[19] C. Lichtensteiger, InteractiveXRDFit: A new tool to simulate and fit x-ray diffractograms of oxide thin films and heterostructures, J. Appl. Crystallogr. **51**, 1745 (2018).

[20] A. Barla, J. Nicolás, D. Cocco, S. M. Valvidares, J. Herrero-Martín, P. Gargiani, J. Moldes, C. Ruget, E. Pellegrin, and S. Ferrer, Design and performance of BOREAS, the beamline for resonant x-ray absorption and scattering experiments at the ALBA synchrotron light source, J. Synchrotron Radiat. **23**, 1507 (2016).

[21] C. Piamonteze, U. Flechsig, S. Rusponi, J. Dreiser, J. Heidler, M. Schmidt, R. Wetter, M. Calvi, T. Schmidt, H. Pruchova, J. Krempasky, C. Quitmann, H. Brune, and F. Nolting, X-Treme beamline at SLS: X-ray magnetic circular and linear dichroism at high field and low temperature, J. Synchrotron Radiat. **19**, 661 (2012).

[22] P. Carra, B. T. Thole, M. Altarelli, and X. Wang, X-ray circular dichroism and local magnetic fields, Phys. Rev. Lett. **70**, 694 (1993).

[23] See Supplemental Material at http://link.aps.org/supplemental/10.1103/PhysRevMaterials.7.104407 for additional data and details on the application of the XMCD sum rules. The Supplemental Material also contains Refs. [31–33].

[24] G. De Luca, J. Spring, U. Bashir, M. Campanini, R. Totani, C. Dominguez, A. Zakharova, M. Döbeli, T. Greber, M. D. Rossell, C. Piamonteze, and M. Gibert, Ferromagnetic insulating epitaxially strained La_2NiMnO_6 thin films grown by sputter deposition, APL Mater. **9**, 081111 (2021).

[25] G. De Luca, J. Spring, M. Kaviani, S. Jöhr, M. Campanini, A. Zakharova, C. Guillemard, J. Herrero-Martin, R. Erni, C. Piamonteze, M. D. Rossell, U. Aschauer, and M. Gibert, Top-layer engineering reshapes charge transfer at polar oxide interfaces, Adv. Mater. **34**, 2203071 (2022).

[26] M. Brahlek, A. K. Choquette, C. R. Smith, R. Engel-Herbert, and S. J. May, Structural refinement of *Pbnm*-type perovskite films from analysis of half-order diffraction peaks, J. Appl. Phys. **121**, 045303 (2017).

[27] P. Reith, X. Renshaw Wang, and H. Hilgenkamp, Analysing magnetism using scanning SQUID microscopy, Rev. Sci. Instrum. **88**, 123706 (2017).

[28] X. R. Wang, C. J. Li, W. M. Lü, T. R. Paudel, D. P. Leusink, M. Hoek, N. Poccia, A. Vailionis, T. Venkatesan, J. M. Coey, E. Y. Tsymbal, Ariando, and H. Hilgenkamp, Imaging and control of ferromagnetism in $LaMnO_3/SrTiO_3$ heterostructures, Science **349**, 716 (2015).

[29] A. Ohtomo and H. Y. Hwang, A high-mobility electron gas at the $LaAlO_3/SrTiO_3$ heterointerface, Nature (London) **427**, 423 (2004).

[30] M. Medarde, A. Fontaine, J. L. García-Muñoz, J. Rodríguez-Carvajal, M. De Santis, M. Sacchi, G. Rossi, and P. Lacorre, $RNiO_3$ perovskites (R=Pr,Nd): Nickel valence and the metal-insulator transition investigated by x-ray-absorption spectroscopy, Phys. Rev. B **46**, 14975 (1992).

[31] J. P. Crocombette, B. T. Thole, and F. Jollet, The importance of the magnetic dipole term in magneto-circular x-ray absorption dichroism for 3d transition metal compounds, J. Phys.: Condens. Matter **8**, 4095 (1996).

[32] T. Saitoh, A. E. Bocquet, T. Mizokawa, and A. Fujimori, Systematic variation of the electronic structure of 3d transition-metal compounds, Phys. Rev. B **52**, 7934 (1995).

[33] C. Piamonteze, P. Miedema, and F. M. F. de Groot, Accuracy of the spin sum rule in XMCD for the transition-metal L edges from manganese to copper, Phys. Rev. B **80**, 184410 (2009).